ACS APPLIED ENERGY MATERIALS
Cite This: ACS Appl. Energy Mater. XXXX, XXX, XXX−XXX
Forum Article
www.acsaem.org

Influence of One Specific Carbon−Carbon Bond on the Quality, Stability, and Photovoltaic Performance of Hybrid Organic−Inorganic Bismuth Iodide Materials

David M. Fabian,[†] Alex M. Ganose,[‡,§,∥] Joseph W. Ziller,[†] David O. Scanlon,[‡,§,∥] Matthew C. Beard,[⊥] and Shane Ardo*[,†,#,△]

[†]Department of Chemistry, University of California, Irvine, California 92697-2025, United States
[‡]Department of Chemistry, University College London, 20 Gordon Street, London WC1H 0AJ, United Kingdom
[§]Diamond Light Source, Harwell Campus, Didcot OX11 0DE, United Kingdom
[∥]Thomas Young Centre, University College London, Gower Street, London WC1E 6BT, United Kingdom
[⊥]National Renewable Energy Laboratory, Golden, Colorado 80401, United States
[#]Department of Materials Science & Engineering, University of California, Irvine, California 92697-2025, United States
[△]Chemical & Biomolecular Engineering, University of California, Irvine, California 92697-2025, United States

Supporting Information

ABSTRACT: Hybrid organic−inorganic halide perovskites are promising materials for thin-film solar cells. However, the toxicity and instability of best-in-class lead−halide perovskite materials make them nonideal. To combat these issues, we replaced lead with bismuth and explored the sensitivity of these new lead-free materials to the valency and bonding of their cationic organic groups. Specifically, we synthesized and characterized the materials properties and photophysical properties of hexane-1,6-diammonium bismuth pentaiodide ($(HDA^{2+})BiI_5$) and compared them to an analogue containing a more volatile organic group with half the number of carbon and nitrogen atoms in the form of *n*-propylammonium ($(PA^{+})_xBiI_{3+x}$, where $1 < x < 3$). The full crystallographic structures of $(HDA^{2+})BiI_5$ and $(PA^{+})_xBiI_{3+x}$ were resolved by single-crystal X-ray diffraction. $(HDA^{2+})BiI_5$ was shown to be pure-phase and have a one-dimensional structure, whereas $(PA^{+})_xBiI_{3+x}$ was shown to be a mix of one-dimensional and zero-dimensional phases. Structures of the materials were confirmed by synchrotron X-ray diffraction of powders. Both $(HDA^{2+})BiI_5$ and $(PA^{+})_xBiI_{3+x}$ exhibit steady-state photoluminescence at room temperature. Density functional theory calculations of $(HDA^{2+})BiI_5$ predict electronic absorption features and a ∼2 eV bandgap that are consistent with those observed experimentally. Structure−property relationships of the materials were examined, and moisture tolerance and film quality were found to be superior for dication-containing $(HDA^{2+})BiI_5$ in relation to monocation-containing $(PA^{+})_xBiI_{3+x}$. We hypothesize that these trends are in part due to a molecular bridging effect enabled by the presence of the dicationic hexanediammonium groups in $(HDA^{2+})BiI_5$. Solar cells fabricated using $(HDA^{2+})BiI_5$ as the photoactive layer exhibited photovoltaic action while those containing $(PA^{+})_xBiI_{3+x}$ did not, suggesting that organic dicationic groups are beneficial to light-absorber morphology and ultimately solar-cell performance.

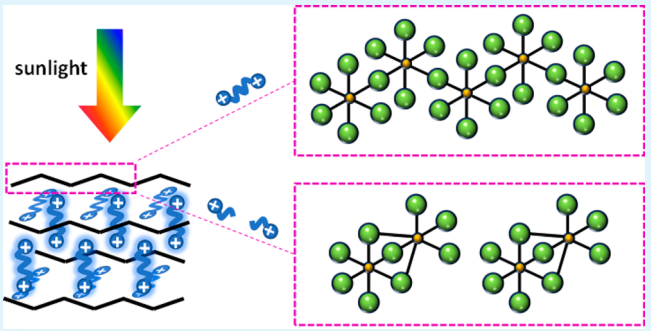

KEYWORDS: *bismuth halide, hybrid organic−inorganic, dications, stability, nontoxic, photovoltaic, solar cells, solar fuels*

INTRODUCTION

Lead-halide-based hybrid organic−inorganic perovskite materials ($APbX_3$) are promising light-absorbers for use in thin-film solar cells due to their low-temperature processability[1−3] and demonstrated laboratory-scale efficiencies of >20%.[4,5] $APbX_3$ has also been incorporated in devices for solar fuels production, where solar-to-hydrogen conversion efficiencies of 2.5% have been reported.[6,7] While application of this new materials class in solar fuels devices may lead to a promising technology, $APbX_3$ is not ideal because it contains toxic lead and the materials are unstable in humid ambient conditions. Compatibility with humid air is the minimum requirement for a solar fuels device that uses water as a clean source of electrons.[8−10] Therefore, research into classes of photoactive materials that are moisture tolerant and are of a high quality is important.

Received: October 20, 2018
Accepted: January 29, 2019

We have previously reported a one-dimensional hybrid organic–inorganic bismuth–halide material, hexane-1,6-diammonium bismuth pentaiodide, $NH_3(CH_3)_6NH_3BiI_5$ ($(HDA^{2+})BiI_5$), for use as the photoactive layer in solar cells.[11] When processed under ambient conditions, this material exhibited superior film quality, photovoltaic performance, and stability in comparison to the widely studied three-dimensional methylammonium lead triiodide. We proposed that the dicationic nature of the organic hexanediammonium groups allowed it to bridge unit cells in the structure and provide increased stability. Evidence for this structural arrangement is supported by single-crystal X-ray structures of these materials reported by Mousdis et al.[12] While some additional studies have been performed using these materials,[13,14] no additional evidence exists that this structural architecture provides increased stability. To further assess this, herein we compare one-dimensional ($(HDA^{2+})BiI_5$, which contains bridging dicationic organic groups, to an analogue that contains only nonbridging monocationic organic *n*-propylammonium (PA^+) groups with half the number of carbon and nitrogen atoms.

In 2000, Mitzi introduced the possibility of using nontoxic lower-dimensional photoactive materials in hybrid organic–inorganic solar cells with the introduction of metal-deficient two-dimensional $(H_2AEQT)Bi_{2/3}I_4$, where AEQT = 5,5‴-bis(aminoethyl)-2,2′:5′,2″:5″,2‴-quaterthiophene.[15] Since then, only two other analogous two-dimensional bismuth-containing materials have been reported: $(NH_4)_3Bi_2I_9$[16] and $(TMP)_{1.5}[Bi_2I_7Cl_2]$, where TMP = *N*,*N*,*N*′,*N*′-tetramethylpiperazine.[17] The all-inorganic analogue, bismuth iodide (BiI_3), also exhibits a two-dimensional layered structure of BiI_6^{3-} octahedra and has been incorporated in solar cells with efficiencies as large as 1.2%.[18−20] Other hybrid bismuth–halide photoactive layers that have been used in solar cells primarily fall into the class of zero-dimensional $A_3Bi_2I_9$ materials, where A = K^+, Rb^+, Cs^+, methylammonium, or formamidinium, and from which solar-cell efficiencies up to 1.64% have been achieved.[21−25] The low dimensionality of the binuclear clusters of zero-dimensional octahedra results in low charge conductivity,[16,26−30] and therefore, it is speculated that the charge-carrier diffusion lengths are much smaller than those measured for hybrid organic–inorganic materials of higher dimensionality.

While our study will help assess whether specific dicationic organic groups are advantageous to materials properties and moisture stability in this class of hybrid organic–inorganic materials, this comparison is only possible in lower-dimensional materials due to charge balancing. Three-dimensional hybrid organic–inorganic analogues only require single cations per unit cell, yet they often result in more efficient solar-cell performance due to the three-dimensional connectivity of the inorganic units, which facilitates charge-carrier conduction.[31] When the dimensionality of the materials is reduced from three, the inorganic units become much more electronically isolated from each other, resulting in poorer electrical conduction.[32] In cases where the electrically insulating organic unit is small enough, weak electronic interactions between the inorganic units still exist,[31] therefore enabling at least moderate conduction and performance. Herein, we report a comparative study using one-dimensional $(HDA^{2+})BiI_5$ that contains divalent organic cations vs an analogous $(PA^+)_xBiI_{3+x}$ material, where $1 < x < 3$, that contains monovalent organic cations that each contain half the number of carbon and nitrogen atoms. Structural information on material powders and thin films, theoretical maximum solar-cell efficiencies, stability, and photophysical properties are compared in order to elucidate structure–property relationships in these hybrid organic–inorganic bismuth–halide materials.

EXPERIMENTAL SECTION

Single-Crystal Growth. Single crystals of $(HDA^{2+})BiI_5$ were grown by vapor diffusion of dichloromethane into a 0.5 M solution of 1:1 molar ratio hexane-1,6-diamine dihydriodide ($HDAI_2$):BiI_3 in a solvent mixture of 4:1 (v/v) *N*,*N*-dimethylformamide (DMF):dimethyl sulfoxide (DMSO), and with $HDAI_2$ in slight excess to ensure there was no residual BiI_3. Single crystals of $(PA^+)_xBiI_{3+x}$ were grown by vapor diffusion of dichloromethane into a 0.5 M solution of 2:1 molar ratio *n*-propylamine hydriodide (PAI):BiI_3 in methanol, with PAI in slight excess to ensure there was no residual BiI_3. For single-crystal growth of $(PA^+)_xBiI_{3+x}$, methanol was chosen as the solvent because single crystals grown in a solvent mixture of 4:1 (v/v) DMF:DMSO were not large enough for single-crystal diffraction measurements. Details on single-crystal X-ray data collection and structure solutions for $(HDA^{2+})BiI_5$ and $(PA^+)_xBiI_{3+x}$ are provided in the Supporting Information. Density functional theory calculations for $(HDA^{2+})BiI_5$ and $(PA^+)_xBiI_{3+x}$ are also provided in the Supporting Information.

Solution Preparation. All chemicals were used as received. Ammonium iodide salts were synthesized by slow addition of hydriodic acid (47% in water, stabilized with 1.5% hypophosphorous acid, Sigma-Aldrich) to either hexane-1,6-diamine (98+%, Alfa Aesar) or *n*-propylamine (98%, Sigma-Aldrich) dissolved in methanol. As an example, to synthesize $HDAI_2$, 260.9 mg of hexane-1,6-diamine was dissolved in 5 mL of methanol, and then 1 mL of hydriodic acid was added slowly at 0 °C with stirring, followed by stirring for an additional 30 min. In this case, the hydriodic acid to amine molar ratio was 2:1, with hydriodic acid in slight excess. $HDAI_2$ precipitate was recovered by evaporation of solvents at 40 °C with a rotary evaporator. The precipitate was rinsed with diethyl ether and vacuum-dried at 60 °C for at least 12 h. An analogous procedure for the preparation of PAI was carried out, but the hydriodic acid to amine molar ratio was 1:1, with hydriodic acid in slight excess. There were 0.5 M solutions of $(HDA^{2+})BiI_5$ and $(PA^+)_xBiI_{3+x}$ then prepared by mixing powders of $HDAI_2$ or PAI with BiI_3 (99.999%, Sigma-Aldrich) at an approximately 1:1 molar ratio, with $HDAI_2$ or PAI in slight excess, in an anhydrous mixture of 4:1 (v/v) DMF:DMSO at 70 °C inside a nitrogen-filled glovebox. The $(HDA^{2+})BiI_5$ and $(PA^+)_xBiI_{3+x}$ solutions were stored in the glovebox until use and were used within 1 week of preparation.

Materials Processing. All steps of materials deposition and solar-cell fabrication were performed in air with 40–60% relative humidity and as described below, unless noted otherwise. All thermal treatments were performed using a hot plate. Fluorine-doped tin–oxide-coated glass (FTO) substrates were cleaned as follows: (1) sonicated in Alconox solution, (2) rinsed with deionized water, (3) rinsed with ethanol, (4) sonicated in ethanol, and (5) dried under nitrogen gas flow. A compact TiO_2 ($cTiO_2$) layer was deposited by pipetting a solution of titanium diisopropoxide bis(acetylacetonate) on a clean FTO substrate, and then the substrate was spun at 2000 rpm (2000 rpm/s acceleration) for 60 s. The substrate was subsequently dried at 125 °C and then sintered at 550 °C for 30 min. Nanoparticles of TiO_2 were synthesized following a procedure by Ito et al.[33] The nanoparticle solution was further diluted in ethanol at a ratio of 1:3.5 (w/w) TiO_2 nanoparticle solution/ethanol to make a mesoporous TiO_2 ($mTiO_2$) suspension. The $mTiO_2$ layer was deposited by spin-coating this solution at 500 rpm (500 rpm/s acceleration) for 5 s and then at 5000 rpm (5000 rpm/s acceleration) for 25 s, followed by drying at 125 °C, and then sintering at 550 °C for 30 min. The substrates were allowed to cool to room temperature. Unless otherwise noted, a conventional spin-coat method was adapted from Kim et al.[34] and used for depositing the hybrid organic–inorganic bismuth–iodide solutions that served as the photoactive

DOI: 10.1021/acsaem.8b01809
ACS Appl. Energy Mater. XXXX, XXX, XXX–XXX

layer. For this method, a filtered solution of $(HDA^{2+})BiI_5$ or $(PA^+)_xBiI_{3+x}$ in 4:1 (v/v) DMF/DMSO was pipetted on top of the $mTiO_2$-coated FTO substrate, and then the substrate was spun at 3000 rpm (3000 rpm/s acceleration) for 60 s, followed by rapid transfer to a hot plate that was preheated to 100 °C and subsequent annealing at 100 °C for 45 min. In most cases, the fast-deposition crystallization method was employed for depositing the $(PA^+)_xBiI_{3+x}$ photoactive layer, which was adapted from Xiao et al.[35] For the fast-deposition crystallization method, the photoactive layer solution was spun at 6000 rpm (6000 rpm/s acceleration) for a total of 30 s, and 6 s before the end of the spin process, anhydrous chlorobenzene was dispensed onto the film while the substrate was spinning. For both photoactive layer deposition methods, the photoactive layer solution was dispensed on the substrate at a volume of 17.5 $\mu L/cm^2$.

Characterization. All samples for characterization were measured under ambient conditions. High-resolution synchrotron powder diffraction data were collected using beamline 11-BM at the Advanced Photon Source at Argonne National Laboratory using a calibrated wavelength of 0.41417 Å. Discrete detectors covering an angular range from −6° to 16° 2θ are scanned over a 34° 2θ range, with data points collected every 0.001° 2θ and scan speed of 0.01°/s. Data are collected while continually scanning the diffractometer 2θ arm. A mixture of NIST standard reference materials, Si (SRM 640c) and Al_2O_3 (SRM 676), is used to calibrate the instrument, where the Si lattice constant determines the wavelength for each detector. Corrections are applied for detector sensitivity, 2θ offset, small differences in wavelength between detectors, and the source intensity, as noted by the ion chamber before merging the data into a single set of intensities evenly spaced in 2θ. For ease of data presentation, 2θ values were adjusted as if Cu Kα radiation (1.5406 Å) was used. Grazing-incidence X-ray diffraction (XRD) data were collected using a Rigaku Smartlab diffractometer with Cu Kα radiation and in parallel beam geometry. Scanning electron microscopy images were acquired on a FEI Magellan 400L XHR using 15 kV accelerating voltage and 0.8 nA beam current. Thermogravimetric analysis data were obtained using a TGA Q500 instrument by TA Instruments. Transmission and reflection spectra were obtained using an integrating sphere in a Shimadzu UV-3600 ultraviolet−visible−near-infrared spectrophotometer. Absorption was calculated by assuming absorptance = 1 − transmittance − reflectance. Steady-state photoluminescence (PL) was measured with a Horiba Jobin Yvon Model FL-1039/40 Fluorolog, a Horiba Jobin Yvon iHR320 spectrograph, and a Horiba Jobin Yvon SPEX Instruments S.A. Group Spectrum One G35 CCD camera. A monochromatized Xe lamp was used as the excitation source. Steady-state PL data were corrected for the wavelength-dependent response of the detection system. Time-resolved photoluminescence spectroscopy measurements were performed using the time-correlated single photon counting technique. Excitation light was generated by a Fianium SC-450-PP laser operating with an average power of 15.5 μW at a repetition rate of 10 MHz and a wavelength of 450 nm selected by a Fianium AOTF system. A 470 nm long pass filter was used to remove scattering from the excitation source. The emission was detected using a Hamamatsu streak camera with a wavelength range of 200−900 nm and response of <20 ps. For a clearer comparison, data were shifted and normalized so that maximal values of 1 occurred at t = 0 ns. To obtain kinetic data, the signal was averaged over the entire spectrum for which there was an appreciable signal (~530−700 nm).

RESULTS AND DISCUSSION

Crystals of $(HDA^{2+})BiI_5$ grew in the form of red needles using vapor deposition from a solvent mixture of 4:1 (v/v) DMF/DMSO, and single-crystal XRD data confirmed the crystal structure (Figure 1). These data also provided evidence that the organic dication (white, blue) bridges iodides (green) coordinated to different bismuth(III) ions (yellow) and yielded one-dimensional chains of corner-sharing octahedra.[11,12] The chains of bismuth−iodide octahedra align

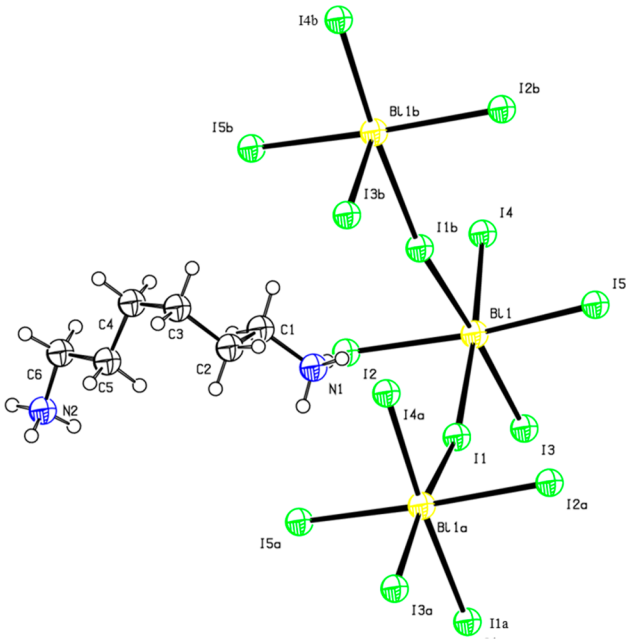

Figure 1. Molecular structure of $(HDA^{2+})BiI_5$, with thermal ellipsoids drawn at the 50% probability level and where green = iodine, yellow = bismuth, blue = nitrogen, and white = carbon.

perpendicularly to the c-axis along the (110) plane, as indicated by the red plane in Figure S1a, which shows a 1 × 1 × 3 unit cell structure of $(HDA^{2+})BiI_5$. The organic hexanediammonium groups in the $(HDA^{2+})BiI_5$ structure are "c"-shaped, supporting the notion that there is some bonding interaction between terminal ammonium groups of hexanediammonium and iodides of BiI_5^{2-} that is causing the hexanediammonium groups to orient. While DMF and DMSO complexation and solvation may hinder single-crystal growth of lead-based perovskite materials, this is not the case for bismuth-based analogues where prior work has shown that solvent combinations similar to ours result in single crystals of BiI_3 and zero-dimensional $A_3Bi_2I_9$ compounds.[27,30,36−38] In Figure S1b, the same structure is displayed but rotated 90°, and in Figure S1c the same orientation of the structure as in Figure S1b is displayed, but with the hexanediammonium groups omitted. Figure S1b,c highlights the inorganic BiI_5^{2-} framework of $(HDA^{2+})BiI_5$ through which rapid charge-carrier conduction takes place.[39] Since the inorganic framework is only one-dimensional, charge-carrier conduction is conjectured to be much faster intrachain along the c-axis than interchain along the a-axis and b-axis. Table S1 shows crystallographic information pertaining to the $(HDA^{2+})BiI_5$ single crystal.

We suspected that comparative monocationic $(PA^+)_xBiI_{3+x}$ crystals would be isostructural to $(HDA^{2+})BiI_5$ crystals. However, it is evident from Figure S2 that the inorganic framework of the $(PA^+)_xBiI_{3+x}$ single crystal is different than that of $(HDA^{2+})BiI_5$, because it contains clusters of $Bi_2I_9^{3-}$ bioctahedra. This structure is zero-dimensional, and therefore, it is much like that of methylammonium bismuth iodide and previously reported $A_3Bi_2I_9$ materials.[27,30,36−38] Table S2 shows crystallographic information pertaining to the $(HDA^{2+})BiI_5$ single crystal.

Synchrotron XRD was performed on $(HDA^{2+})BiI_5$ powders obtained by mechanical abrasion of spin-coated thin films (Figure 2a, red line). The diffraction patterns are consistent with the calculated powder pattern based on the single-crystal

DOI: 10.1021/acsaem.8b01809
ACS Appl. Energy Mater. XXXX, XXX, XXX−XXX

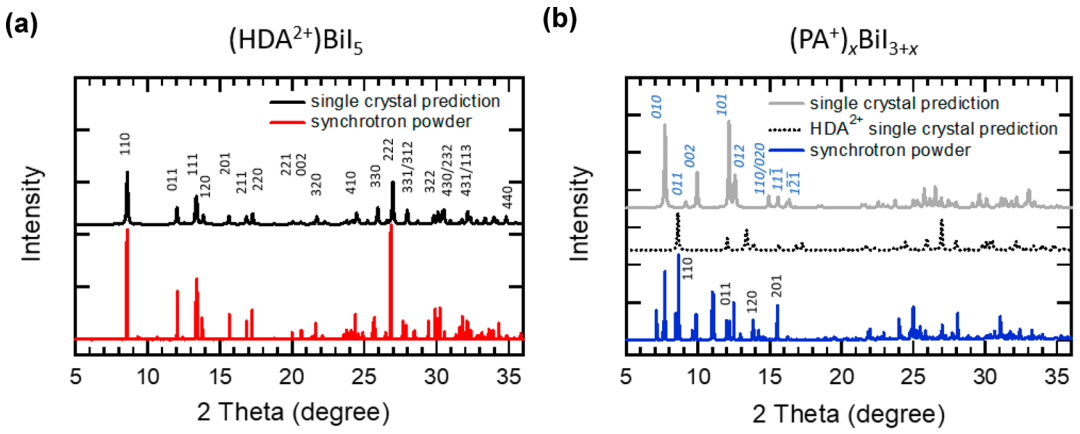

Figure 2. X-ray diffraction patterns of (a) $(HDA^{2+})BiI_5$ and (b) $(PA^+)_xBiI_{3+x}$ measured for powders obtained by mechanical abrasion of spin-coated thin films using a synchrotron source (red and blue lines, respectively) and predicted from the resolved single-crystal structure (black and gray lines, respectively). For ease of comparison, in panel b the black dotted line and black text are reflections predicted from the resolved single-crystal structure of $(HDA^{2+})BiI_5$ shown in panel a.

data (Figure 2a, black line). The similarity in these diffraction patterns supports that the $(HDA^{2+})BiI_5$ single crystal that is seeded from solution has the same structure as the $(HDA^{2+})BiI_5$ thin film that crystallizes during annealing. Figure 2b displays the same comparison in XRD patterns for $(PA^+)_xBiI_{3+x}$. It is evident that other crystal phases are present in the $(PA^+)_xBiI_{3+x}$ powder scraped off from thin films in addition to the single-crystal phase that grew in solution (Figure S2). In Figure 2b, the peaks labeled in black font correspond to the one-dimensional phase that matches that of $(HDA^{2+})BiI_5$, which includes peaks at 2θ = 8.65° (110), 12.0° (011), 13.8° (120), and 15.5° (201), and the peaks labeled in blue font correspond to the zero-dimensional phase that matches the resolved single-crystal structure. The unlabeled peaks present in the XRD data presented in Figure 2b are suspected to correspond to undetermined phases. These peaks may be attributed to crystalline phases that formed during transportation to or measurement by the bright synchrotron source.

Grazing-incidence XRD data of annealed thin films are presented in Figure 3. The XRD pattern of the $(HDA^{2+})BiI_5$ thin film (Figure 3, red line) matches the patterns of the single crystal and powders presented in Figure 2, indicating a phase-pure one-dimensional framework of corner-sharing bismuth−iodide octahedra. For the thin-film XRD pattern of $(PA^+)_xBiI_{3+x}$ (Figure 3, blue line), however, the dominant peak at ∼7.4° is indexed to the (010) peak of single-crystal $(PA^+)_xBiI_{3+x}$, which corresponds to the zero-dimensional phase of the material. Our data suggest that annealed thin films of $(PA^+)_xBiI_{3+x}$ contain a mixture of a one-dimensional phase of corner-sharing bismuth−iodide octahedra analogous to $(HDA^{2+})BiI_5$ and a zero-dimensional phase containing clusters of bismuth−iodide bioctahedra analogous to $A_3Bi_2I_9$ materials. The similarity between the thin-film XRD pattern of $(PA^+)_xBiI_{3+x}$ cast from 4:1 (v/v) DMF/DMSO and neat methanol (Figure S3) suggests that the complex XRD pattern does not arise from the choice of solvent. Moreover, because grazing-incidence XRD only resolves peaks that are preferentially oriented, a number of the reflections determined for $(PA^+)_xBiI_{3+x}$ by synchrotron XRD (Figure 2b) do not show an appreciable signal in the grazing-incidence XRD pattern.

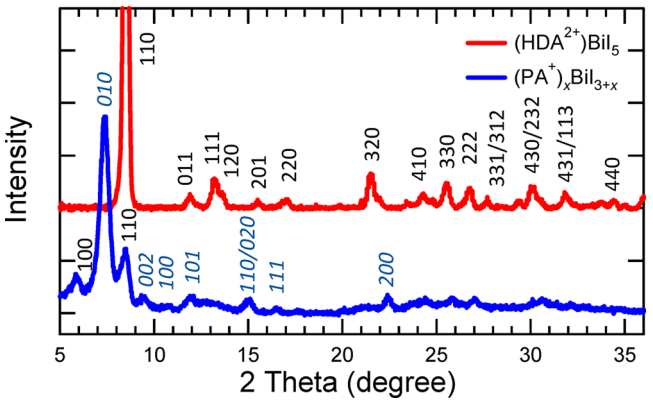

Figure 3. Grazing-incidence X-ray diffraction patterns of thin films of $(HDA^{2+})BiI_5$ (red line, black text) and $(PA^+)_xBiI_{3+x}$ (blue line, blue text) on fluorine-doped tin−oxide-coated glass. The pattern matches well with that obtained for $(HDA^{2+})BiI_5/TiO_2/FTO$ reported in ref 11, but $(HDA^{2+})BiI_5$ peaks have now been more accurately indexed on the basis of the single-crystal structure determined in Figure 1.

Density functional theory (DFT) calculations were performed to investigate the optoelectronic properties of $(HDA^{2+})BiI_5$ (Figure 4). The HSE06 hybrid functional was employed with spin−orbit coupling effects explicitly included for all calculations. HSE06 has been shown to reproduce the lattice parameters and bandgaps of many lead−halide-based and bismuth−halide-based materials.[40−42] The indirect and direct bandgaps of $(HDA^{2+})BiI_5$ were calculated to be 2.01 and 2.03 eV, respectively, in very good agreement with our previously published experimentally measured values of 2.05 and 2.15 eV, respectively.[11] Inclusion of spin−orbit coupling was found to lower the calculated bandgap of $(HDA^{2+})BiI_5$ by 0.68 eV, due to the presence of heavy 6p ions.[42] The calculated nonparabolic effective masses of the valence-band maximum and conduction-band minimum are smaller for electrons than holes such that they are $0.57m_0$ at Γ and $2.08m_0$ at Y for electrons and $0.79m_0$ at Γ and $5.80m_0$ at Z for holes, where m_0 = 9.11×10^{-31} kg and is the free electron rest mass.

The calculated optical absorption spectrum of $(HDA^{2+})BiI_5$ agrees well with our previously published electronic absorption data,[11] in that $(HDA^{2+})BiI_5$ shows a similarly large absorption coefficient just above its bandgap (Figure S4). Strong optical absorption is beneficial to solar-cell performance, and for this reason, we calculated the spectroscopy-limited maximum

DOI: 10.1021/acsaem.8b01809
ACS Appl. Energy Mater. XXXX, XXX, XXX−XXX

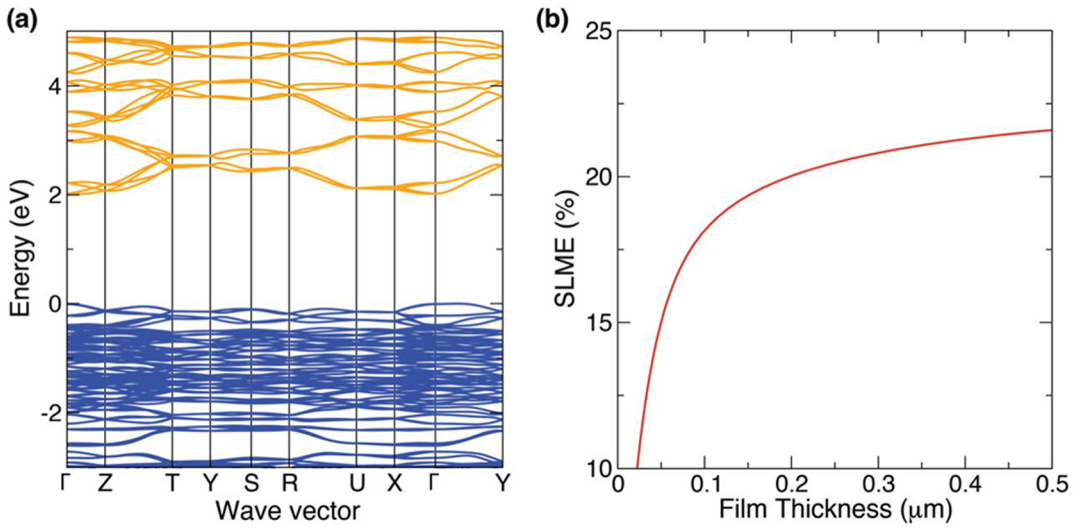

Figure 4. (a) HSE06+SOC band structure of $(HDA^{2+})BiI_5$, with the valence-band maximum set equal to 0 eV. (b) Calculated spectroscopy-limited maximum efficiency (SLME) of $(HDA^{2+})BiI_5$.

efficiency (SLME),[43−46] which is a metric to predict the maximum solar-cell efficiency considering the direct/indirect nature of the bandgap, the strength of optical absorption, and the thickness of the film. For $(HDA^{2+})BiI_5$ the efficiency was calculated to be >20% for film thicknesses of >∼250 nm (Figure 4b). This is very close to the Shockley−Queisser detailed-balance limit of 21.6% for a material with a similar bandgap of 2.05 eV and suggests that if the $(HDA^{2+})BiI_5$ photoactive layer has a quantum yield for emission of unity and the solar cell has optimal selective contacts, we can approach this efficiency limit.

Electronic absorption and steady-state photoluminescence spectra of thin films of $(HDA^{2+})BiI_5$ and $(PA^+)_xBiI_{3+x}$ are displayed in Figure 5. The more gradual and hypsochromic

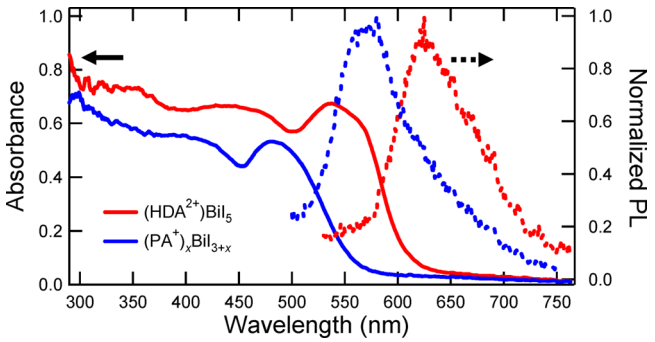

Figure 5. Absorption spectra (solid lines) and steady-state photoluminescence (PL) spectra using excitation at 400 nm (dashed lines) for thin films of $(HDA^{2+})BiI_5$ (red lines) and $(PA^+)_xBiI_{3+x}$ (blue lines).

absorption onset of $(PA^+)_xBiI_{3+x}$ compared to $(HDA^{2+})BiI_5$ supports the XRD data that the $(PA^+)_xBiI_{3+x}$ film is composed of a mix of one-dimensional and zero-dimensional phases. Near-band-edge photoluminescence is present from both materials suggesting that the emission is not from intragap trap states.[47] It is also evident in Figure S5 that there is no wavelength-dependent response to the emission of each film, indicating that the observed signal is not due to a scattering phenomenon.

Time-resolved photoluminescence measurements were carried out on $(HDA^{2+})BiI_5$ and $(PA^+)_xBiI_{3+x}$ thin films. A transient signal above the instrument response was only obtained for the $(HDA^{2+})BiI_5$ thin film when 10 wt % KI was incorporated in the precursor solution, and the measured photoluminescence lifetime was <1 ns (Figure S6a). Incorporation of KI was motivated by Stranks and colleagues who reported that KI removed defects and therefore increased emission from lead-halide-based perovskite thin films.[48] Time-resolved photoluminescence spectra of the $(HDA^{2+})BiI_5$ thin film with 10 wt % KI incorporation are shown in Figure S6b. The spectra represent time regions that are prior to signal decay when there is primarily scattering off of the sample (black line), during the initial signal decay (red line), and during all of the signal decay out to 0.8 ns (green line). Signals beyond the first scattering time region are predominantly observed in the wavelength range 580−650 nm, which matches the range of maximum steady-state emission intensity.

The determination of an ideal solution deposition method for the hybrid bismuth−iodide materials under investigation was challenging, and a single solution-deposition method was not identified that yielded the highest-quality film for both materials. This is evident in the (absorptance + reflectance) spectral data presented in Figure S7, where less scattering at long wavelengths and larger absorbance is desired. With the assumption of identical thicknesses, values for the absorptance should be the same regardless of deposition method. It is clear, therefore, that reflectance is larger for the $(HDA^{2+})BiI_5$ film processed using the fast-deposition crystallization method with chlorobenzene as the antisolvent (red dashed line) than for the $(HDA^{2+})BiI_5$ film processed by the one-step deposition technique (red solid line). This is evident by the fact that, for the $(HDA^{2+})BiI_5$ film processed using the fast-deposition crystallization method, values of (absorptance + reflectance) at wavelengths longer than the absorption onset (i.e., >∼625 nm) are larger than those for the $(HDA^{2+})BiI_5$ film processed by the one-step technique. However, the opposite is true for $(PA^+)_xBiI_{3+x}$ (blue lines). Greater reflectance suggests larger scattering effects of the film that can in part be attributed to poorer film coverage on the substrate.

DOI: 10.1021/acsaem.8b01809
ACS Appl. Energy Mater. XXXX, XXX, XXX−XXX

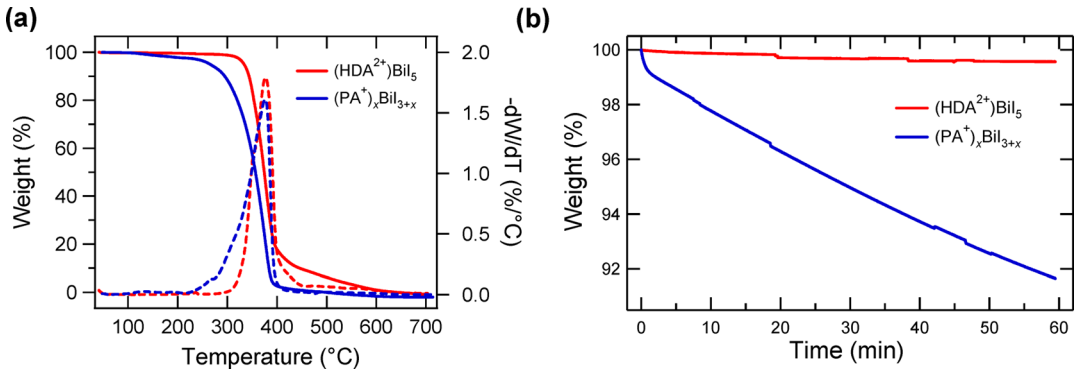

Figure 6. Thermogravimetric analysis of $(HDA^{2+})BiI_5$ and $(PA^+)_xBiI_{3+x}$ powders as a function of (a) temperature at a ramp rate of 20 °C/min and (b) time at 200 °C. In panel a, the solid curves correspond to the % mass remaining (left axis), and the dashed curves correspond to the derivative of the % mass with respect to temperature (right axis).

The disparity in absorption onset and film color can also be explained through differences in thin-film coverage. It is evident from plan-view scanning electron microscopy images of $(HDA^{2+})BiI_5$ (Figure S8a,b) and $(PA^+)_xBiI_{3+x}$ (Figure S8c,d) that, even though both material thin films consist of lamellar structures, the surface coverage of $(HDA^{2+})BiI_5$ on a TiO_2/FTO substrate is larger than that for $(PA^+)_xBiI_{3+x}$. The reason for this discrepancy is still unknown, but it is conjectured that the organic dicationic hexanediammonium groups bridge the chains of bismuth−iodide octahedra more effectively than the organic monocationic propylammonium groups. For a given spin-coat speed, acceleration, and time (3000 rpm, 1 rpm/s acceleration, 60 s) as well as concentration (1 M) in the 4:1 (v/v) DMF/DMSO solution, it is clear that the extent of visible-light absorption by the $(HDA^{2+})BiI_5$ thin film is far superior to that by the $(PA^+)_xBiI_{3+x}$ thin film (Figure S9).

The thermal stabilities of $(HDA^{2+})BiI_5$ and $(PA^+)_xBiI_{3+x}$ powders were assessed by thermogravimetric analysis (Figure 6). The onset of significant mass loss occurs at a lower temperature for $(PA^+)_xBiI_{3+x}$ (<250 °C) than for $(HDA^{2+})BiI_5$ (>300 °C), which is depicted in the derivative plots of Figure 6a (dashed lines). It is also evident in Figure 6a that there is a nonzero slope of the mass loss curve of $(PA^+)_xBiI_{3+x}$ (blue solid line) even at temperatures below 200 °C whereas the mass loss curve of $(HDA^{2+})BiI_5$ is flatter (red solid line). This difference is accentuated in the ramp-and-hold thermogravimetric data displayed in Figure 6b, where the temperature in the thermogravimetric chamber was ramped to 200 °C and then held and monitored at 200 °C. After 1 h, the $(PA^+)_xBiI_{3+x}$ powder sample lost ∼8% of its original mass whereas the $(HDA^{2+})BiI_5$ powder sample lost only ∼0.5% of its original mass. The greater thermal stability of $(HDA^{2+})BiI_5$ compared to that of $(PA^+)_xBiI_{3+x}$ can be rationalized by differences in boiling points of the precursors of the organic groups. The boiling point of hexane-1,6-diamine is 204 °C, and the boiling point of *n*-propylamine is 49 °C. In addition, part of the superior stability of $(HDA^{2+})BiI_5$ could be explained by a molecular bridging effect, where organic dicationic hexanediammonium groups give $(HDA^{2+})BiI_5$ more structural rigidity than the organic monocationic propylammonium groups give $(PA^+)_xBiI_{3+x}$.

Solar cells were fabricated with the architecture Au/spiro-OMeTAD/Bi/$mTiO_2$/ALD-$cTiO_2$/FTO, where spiro-OMeTAD is 2,2′,7,7′-tetrakis(*N*,*N*′-di-*p*-methoxyphenylamine)-9,9′-spirobifluorene, Bi is either $(HDA^{2+})BiI_5$ or $(PA^+)_xBiI_{3+x}$, and ALD-$cTiO_2$ is compact TiO_2 deposited via atomic layer deposition. The $cTiO_2$ layer was deposited by atomic layer deposition, instead of by solution deposition, because poor solar-cell performance from cells using solution-deposited $cTiO_2$ was hypothesized to be due to incomplete coverage of the FTO substrate. Current density versus potential behaviors of our best-performing solar cells with $(HDA^{2+})BiI_5$ or $(PA^+)_xBiI_{3+x}$ as the photoactive layer and with an ALD-$cTiO_2$ layer are shown in Figure 7. The smaller magnitude of

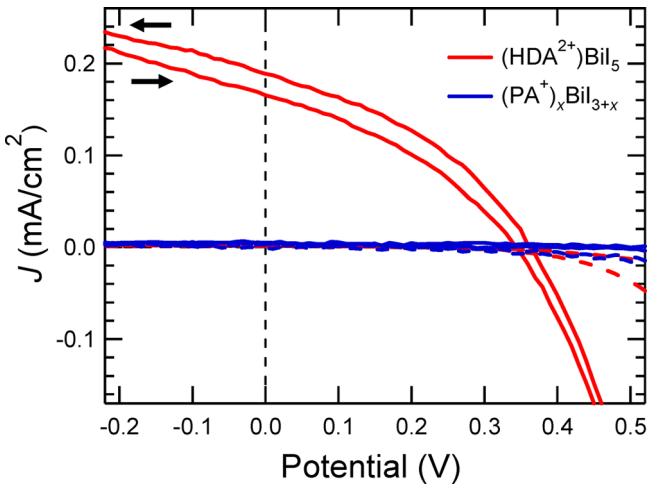

Figure 7. Current density (J) vs potential data at a scan rate of 100 mV/s for complete solar cells consisting of Au/spiro-OMeTAD/Bi/$mTiO_2$/ALD-$cTiO_2$/FTO, where Bi is $(HDA^{2+})BiI_5$ (red lines) or $(PA^+)_xBiI_{3+x}$ (blue lines), $mTiO_2$ is mesoporous TiO_2, and ALD-$cTiO_2$ is atomic-layer-deposited compact TiO_2. Solid lines are from measurements performed under simulated 1 Sun illumination, with sweep directions indicated by arrows, and dashed lines are from measurements performed in the dark.

the reverse saturation dark current density in comparison to our previous data using solution-deposited $cTiO_2$ suggests that the atomic layer deposition protocol was beneficial.[11] Solar cells containing $(HDA^{2+})BiI_5$ had an active area of 0.25 cm^2, and data from three solar cells (mean ± standard deviation), each obtained from the reverse sweeps, exhibited an open-circuit photovoltage of 340 ± 30 mV, a short-circuit photocurrent density of 0.15 ± 0.04 mA cm^{-2}, and a power-conversion efficiency of 0.019 ± 0.007% (Figure 7, red line). All three solar cells incorporating $(PA^+)_xBiI_{3+x}$ as the

DOI: 10.1021/acsaem.8b01809
ACS Appl. Energy Mater. XXXX, XXX, XXX−XXX

photoactive layer exhibited no appreciable photocurrent (Figure 7, blue line), which is attributed to a combination of inferior zero-dimensional structure of $(PA^+)_xBiI_{3+x}$ in comparison to that of one-dimensional $(HDA^{2+})BiI_5$ and poor crystallization of $(PA^+)_xBiI_{3+x}$ on the underlying $mTiO_2$ layer as evidenced by plan-view scanning electron microscopy images (Figure S8c,d).

CONCLUSIONS

A comparative study was performed on a hybrid organic−inorganic bismuth−halide material that contained divalent organic cations vs an analogous material containing monovalent organic cations. The crystal structures of dicationic $(HDA^{2+})BiI_5$ and monocationic $(PA^+)_xBiI_{3+x}$, where $1 < x < 3$, were resolved and shown to differ in that $(HDA^{2+})BiI_5$ was orthorhombic and one-dimensional and $(PA^+)_xBiI_{3+x}$ was triclinic and zero-dimensional. Density functional theory calculations supported experimental absorption data for $(HDA^{2+})BiI_5$ and also predicted the bandgap to equal ∼2 eV. Relationships between structure and material characteristics such as photophysical properties, stability, and film quality were investigated. Appreciable steady-state photoluminescence was observed at room temperature for each of the bismuth−halide materials measured, while a time-resolved photoluminescence signal on the 100-picosecond and longer time scales was only apparent for $(HDA^{2+})BiI_5$ thin films and only when KI was incorporated into the precursor solution. $(HDA^{2+})BiI_5$ was shown to be more stable to thermal treatments than $(PA^+)_xBiI_{3+x}$, and film coverage of $(HDA^{2+})BiI_5$ on a TiO_2-coated FTO substrate was superior to that of $(PA^+)_xBiI_{3+x}$. Improved film quality and robustness provide rationale for the use of dicationic organic groups as replacements for monocationic organic groups in hybrid organic−inorganic materials. The dicationic materials exhibited photovoltaic action and an open-circuit photovoltage of ∼340 mV, while the monocationic analogues showed no apparent photoresponse.

ASSOCIATED CONTENT

Supporting Information

The Supporting Information is available free of charge on the ACS Publications website at DOI: 10.1021/acsaem.8b01809.

Additional experimental details, structure solution definitions, density functional theory calculations for $(HDA^{2+})BiI_5$, and Figures S1−S9 and Tables S1 and S2 contain additional characterization data (PDF)

X-ray data collection and structure solution for $(HDA^{2+})BiI_5$ (CIF)

X-ray data collection and structure solution for $(PA^+)_xBiI_{3+x}$ (CIF)

Special Issue Paper

This paper is an additional Forum Article for *ACS Appl. Energy Mater.* **2019**, *2*, issue 1, "New Chemistry to Advance the Quest for Sustainable Solar Fuels".

AUTHOR INFORMATION

Corresponding Author

*E-mail: ardo@uci.edu.

ORCID

David O. Scanlon: 0000-0001-9174-8601

Matthew C. Beard: 0000-0002-2711-1355

Shane Ardo: 0000-0001-7162-6826

Notes

The authors declare no competing financial interest.

ACKNOWLEDGMENTS

D.M.F. and S.A. acknowledge support from the Alfred P. Sloan Foundation under Grant FG-2017-8888 and the School of Physical Sciences at the University of California, Irvine. D.M F. acknowledges support by the DOE, Office of Science, Office of Workforce Development for Teachers and Scientists, Office of Science Graduate Student Research (SCGSR) program under Contract DE SC0014664 and by the National Science Foundation Graduate Research Fellowship under Grant DGE-1321846. D.O.S. acknowledges support from the EPSRC (EP/N01572X/1) and membership of the Materials Design Network. A.M.G. acknowledges Diamond Light Source for the cosponsorship of a studentship on the EPSRC Centre for Doctoral Training in Molecular Modelling and Materials Science (EP/L015862/1). This work made use of the ARCHER UK National Supercomputing Service (http://www.archer.ac.uk), via our membership in the UK's HEC Materials Chemistry Consortium, which is funded by EPSRC (EP/L000202), and the UCL Legion and Grace HPC Facilities. M.C.B. acknowledges support as part of the Center for Hybrid Organic Inorganic Semiconductors for Energy, an Energy Frontier Research Center funded by the Office of Basic Energy Sciences, Office of Science within the U.S. Department of Energy. Work at the National Renewable Energy Laboratory (NREL) was performed under contract DE-AC36-08GO28308 from the U.S. Department of Energy to NREL. Synchrotron X-ray diffraction was performed on the 11-BM beamline at the Advanced Photon Source at Argonne National Laboratory by beamline staff. Use of the Advanced Photon Source at Argonne National Laboratory was supported by the U.S. Department of Energy, Office of Science, Office of Basic Energy Sciences, under Contract DE-AC02-06CH11357. Scanning electron microscopy and X-ray diffraction measurements were performed at the UC Irvine Materials Research Institute. The authors thank Dr. Qiyin Lin (UC Irvine) for guidance in X-ray diffraction data analysis and Austin Ryan (UC Irvine) for assistance with single-crystal X-ray diffraction data acquisition and analysis.

ABBREVIATIONS

$APbX_3$, lead-halide-based hybrid organic−inorganic perovskite
$(HDA^{2+})BiI_5$, hexane-1,6-diammonium bismuth pentaiodide
$(PA^+)_xBiI_{3+x}$, *n*-propylammonium bismuth iodide
$HDAI_2$, hexane-1,6-diamine dihydriodide
PAI, *n*-propylamine hydriodide
v/v, volume/volume ratio
DMF, *N*,*N*-dimethylformamide
DMSO, dimethyl sulfoxide
FTO, fluorine-doped tin−oxide-coated glass
$cTiO_2$, compact titanium dioxide
$mTiO_2$, mesoporous titanium dioxide
XRD, X-ray diffraction
ALD-$cTiO_2$, compact titanium dioxide deposited by atomic layer deposition

DOI: 10.1021/acsaem.8b01809
ACS Appl. Energy Mater. XXXX, XXX, XXX−XXX

REFERENCES

(1) Mitzi, D. B. Templating and Structural Engineering in Organic−Inorganic Perovskites. *J. Chem. Soc. Dalt. Trans.* **2001**, 1−12.

(2) Liu, D.; Kelly, T. L. Perovskite Solar Cells with a Planar Heterojunction Structure Prepared Using Room-Temperature Solution Processing Techniques. *Nat. Photonics* **2014**, *8*, 133−138.

(3) Giustino, F.; Snaith, H. J. Toward Lead-Free Perovskite Solar Cells. *ACS Energy Letters* **2016**, *1*, 1233−1240.

(4) Green, M. A.; Hishikawa, Y.; Dunlop, E. D.; Levi, D. H.; Hohl-Ebinger, J.; Ho-Baillie, A. W. Y. Solar Cell Efficiency Tables (Version 51). *Prog. Photovoltaics* **2018**, *26*, 3−12.

(5) Seok, S. I.; Grätzel, M.; Park, N.-G. Methodologies toward Highly Efficient Perovskite Solar Cells. *Small* **2018**, *14*, 1704177.

(6) Crespo-Quesada, M.; Pazos-Outón, L. M.; Warnan, J.; Kuehnel, M. F.; Friend, R. H.; Reisner, E. Metal-Encapsulated Organolead Halide Perovskite Photocathode for Solar-Driven Hydrogen Evolution in Water. *Nat. Commun.* **2016**, *7*, 6−12.

(7) Chen, Y. S.; Manser, J. S.; Kamat, P. V. All Solution-Processed Lead Halide Perovskite-$BiVO_4$ Tandem Assembly for Photolytic Solar Fuels Production. *J. Am. Chem. Soc.* **2015**, *137*, 974−981.

(8) Spurgeon, J. M.; Lewis, N. S. Proton Exchange Membrane Electrolysis Sustained by Water Vapor. *Energy Environ. Sci.* **2011**, *4*, 2993−2998.

(9) Kumari, S.; Turner White, R.; Kumar, B.; Spurgeon, J. M. Solar Hydrogen Production from Seawater Vapor Electrolysis. *Energy Environ. Sci.* **2016**, *9*, 1725−1733.

(10) Xiang, C.; Chen, Y.; Lewis, N. S. Modeling an Integrated Photoelectrolysis System Sustained by Water Vapor. *Energy Environ. Sci.* **2013**, *6*, 3713.

(11) Fabian, D. M.; Ardo, S. Hybrid Organic−Inorganic Solar Cells Based on Bismuth Iodide and 1,6-Hexanediammonium Dication. *J. Mater. Chem. A* **2016**, *4*, 6837−6841.

(12) Mousdis, G. A.; Papavassiliou, G. C.; Terzis, A.; Raptopoulou, C. P. Preparation, Structures and Optical Properties of $HDABiX_5$ and $HDASbX_5$. *Z. Naturforsch., B: J. Chem. Sci.* **1998**, *53b*, 927−931.

(13) Mitzi, D. B.; Prikas, M. T.; Chondroudis, K. Thin Film Deposition of Organic−Inorganic Hybrid Materials Using a Single Source Thermal Ablation Technique. *Chem. Mater.* **1999**, *11*, 542−544.

(14) Mitzi, D. B.; Brock, P. Structure and Optical Properties of Several Organic−Inorganic Hybrids Containing Corner-Sharing Chains of Bismuth Iodide Octahedra. *Inorg. Chem.* **2001**, *40*, 2096−2104.

(15) Mitzi, D. B. Organic-Inorganic Perovskites Containing Trivalent Metal Halide Layers: The Templating Influence of the Organic Cation Layer. *Inorg. Chem.* **2000**, *39*, 6107−6113.

(16) Sun, S.; Tominaka, S.; Lee, J.-H.; Xie, F.; Bristowe, P. D.; Cheetham, A. K. Synthesis, Crystal Structure, and Properties of a Perovskite-Related Bismuth Phase, $(NH_4)_3\ Bi_2\ I_9$. *APL Mater.* **2016**, *4*, 031101.

(17) Li, M. Q.; Hu, Y. Q.; Bi, L. Y.; Zhang, H. L.; Wang, Y.; Zheng, Y. Z. Structure Tunable Organic−Inorganic Bismuth Halides for an Enhanced Two-Dimensional Lead-Free Light-Harvesting Material. *Chem. Mater.* **2017**, *29*, 5463−5467.

(18) Brandt, R. E.; Kurchin, R. C.; Hoye, R. L. Z.; Poindexter, J. R.; Wilson, M. W. B.; Sulekar, S.; Lenahan, F.; Yen, P. X. T.; Stevanovic, V.; Nino, J. C.; Bawendi, M. G.; Buonassisi, T. Investigation of Bismuth Triiodide (BiI_3) for Photovoltaic Applications. *J. Phys. Chem. Lett.* **2015**, *6*, 4297−4302.

(19) Hamdeh, U. H.; Nelson, R. D.; Ryan, B. J.; Bhattacharjee, U.; Petrich, J. W.; Panthani, M. G. Solution-Processed BiI_3 Thin Films for Photovoltaic Applications: Improved Carrier Collection via Solvent Annealing. *Chem. Mater.* **2016**, *28*, 6567−6574.

(20) Tiwari, D.; Alibhai, D.; Fermin, D. J. Above 600 mV Open Circuit Voltage BiI_3 Solar Cells. *ACS Energy Lett.* **2018**, *3*, 1882−1886.

(21) Park, B.-W.; Philippe, B.; Zhang, X.; Rensmo, H.; Boschloo, G.; Johansson, E. M. J. Bismuth Based Hybrid Perovskites $A_3Bi_2I_9$ (A: Methylammonium or Cesium) for Solar Cell Application. *Adv. Mater.* **2015**, *27*, 6806−6813.

(22) Lehner, A. J.; Fabini, D. H.; Evans, H. A.; Hébert, C.-A.; Smock, S. R.; Hu, J.; Wang, H.; Zwanziger, J. W.; Chabinyc, M. L.; Seshadri, R. Crystal and Electronic Structures of Complex Bismuth Iodides $A_3Bi_2I_9$ (A = K, Rb, Cs) Related to Perovskite: Aiding the Rational Design of Photovoltaics. *Chem. Mater.* **2015**, *27*, 7137−7148.

(23) Huang, X.; Huang, S.; Biswas, P.; Mishra, R. Band Gap Insensitivity to Large Chemical Pressures in Ternary Bismuth Iodides for Photovoltaic Applications. *J. Phys. Chem. C* **2016**, *120*, 28924−28932.

(24) Kamminga, M. E.; Stroppa, A.; Picozzi, S.; Chislov, M.; Zvereva, I. A.; Baas, J.; Meetsma, A.; Blake, G. R.; Palstra, T. T. M. Polar Nature of $(CH_3\ NH_3)_3\ Bi_2\ I_9$ Perovskite-Like Hybrids. *Inorg. Chem.* **2017**, *56*, 33−41.

(25) Zhang, Z.; Li, X.; Xia, X.; Wang, Z.; Huang, Z.; Lei, B.; Gao, Y. High-Quality $(CH_3\ NH_3)_3\ Bi_2\ I_9$ Film-Based Solar Cells: Pushing Efficiency up to 1.64%. *J. Phys. Chem. Lett.* **2017**, *8*, 4300−4307.

(26) Kodzasa, T.; Ushijima, H.; Matsuda, H.; Kamata, T. Preparation of Thin Film of Layer Structured Bismuth Iodide with a Long Chain Alkylammonium and Its Nonlinear Optical Property. *Mol. Cryst. Liq. Cryst. Sci. Technol., Sect. A* **2000**, *343*, 71−75.

(27) Hoye, R.; Brandt, R. E.; Osherov, A.; Stevanovic, V.; Stranks, S. D.; Wilson, M. W. B.; Kim, H.; Akey, A. J.; Kurchin, R. C.; Poindexter, J. R.; Wang, E. N.; Bawendi, M. G.; Bulovic, V.; Buonassisi, T.; Perkins, J. D. Methylammonium Bismuth Iodide as a Lead-Free, Stable Hybrid Organic-Inorganic Solar Absorber. *Chem. - Eur. J.* **2016**, *22*, 2605−2610.

(28) Scholz, M.; Flender, O.; Oum, K.; Lenzer, T. Pronounced Exciton Dynamics in the Vacancy-Ordered Bismuth Halide Perovskite $(CH_3NH_3)_3Bi_2I_9$ Observed by Ultrafast UV−Vis−NIR Transient Absorption Spectroscopy. *J. Phys. Chem. C* **2017**, *121*, 12110−12116.

(29) Kulkarni, A.; Singh, T.; Ikegami, M.; Miyasaka, T. Photovoltaic Enhancement of Bismuth Halide by *N*-Methyl Pyrrolidone-Assisted Morphology Conversion. *RSC Adv.* **2017**, *7*, 9456−9460.

(30) Chen, X.; Myung, Y.; Thind, A.; Gao, Z.; Yin, B.; Shen, M.; Cho, S. B.; Cheng, P.; Sadtler, B.; Mishra, R.; Banerjee, P. Atmospheric Pressure Chemical Vapor Deposition of Methylammonium Bismuth Iodide Thin Films. *J. Mater. Chem. A* **2017**, *5*, 24728−24739.

(31) Papavassiliou, G. C. Three- and Low-Dimensional Inorganic Semiconductors. *Prog. Solid State Chem.* **1997**, *25*, 125−270.

(32) Misra, R. K.; Cohen, B.-E.; Iagher, L.; Etgar, L. Low Dimensional Organic−Inorganic Halide Perovskite: Structure, Properties, and Applications. *ChemSusChem* **2017**, *10*, 3712−3721.

(33) Ito, S.; Murakami, T. N.; Comte, P.; Liska, P.; Grätzel, C.; Nazeeruddin, M. K.; Grätzel, M. Fabrication of Thin Film Dye Sensitized Solar Cells with Solar to Electric Power Conversion Efficiency over 10%. *Thin Solid Films* **2008**, *516*, 4613−4619.

(34) Kim, H.-S.; Lee, C.-R.; Im, J.-H.; Lee, K.-B.; Moehl, T.; Marchioro, A.; Moon, S.-J.; Humphry-Baker, R.; Yum, J.-H.; Moser, J. E.; Grätzel, M.; Park, N.-G. Lead Iodide Perovskite Sensitized All-Solid-State Submicron Thin Film Mesoscopic Solar Cell with Efficiency Exceeding 9%. *Sci. Rep.* **2012**, *2*, 591.

(35) Xiao, M.; Huang, F.; Huang, W.; Dkhissi, Y.; Zhu, Y.; Etheridge, J.; Gray-Weale, A.; Bach, U.; Cheng, Y.-B.; Spiccia, L. A Fast Deposition-Crystallization Procedure for Highly Efficient Lead Iodide Perovskite Thin-Film Solar Cells. *Angew. Chem.* **2014**, *126*, 10056−10061.

(36) Pazoki, M.; Johansson, M. B.; Zhu, H.; Broqvist, P.; Edvinsson, T.; Boschloo, G.; Johansson, E. M. J. Bismuth Iodide Perovskite Materials for Solar Cell Applications: Electronic Structure, Optical Transitions, and Directional Charge Transport. *J. Phys. Chem. C* **2016**, *120*, 29039−29046.

(37) Ran, C.; Wu, Z.; Xi, J.; Yuan, F.; Dong, H.; Lei, T.; He, X.; Hou, X. Construction of Compact Methylammonium Bismuth Iodide Film Promoting Lead-Free Inverted Planar Heterojunction Organohalide Solar Cells with Open-Circuit Voltage over 0.8 V. *J. Phys. Chem. Lett.* **2017**, *8*, 394−400.

DOI: 10.1021/acsaem.8b01809
ACS Appl. Energy Mater. XXXX, XXX, XXX−XXX

(38) Jain, A.; Voznyy, O.; Sargent, E. H. High-Throughput Screening of Lead-Free Perovskite-like Materials for Optoelectronic Applications. *J. Phys. Chem. C* **2017**, *121*, 7183−7187.
(39) Lyu, M.; Yun, J. H.; Cai, M.; Jiao, Y.; Bernhardt, P. V.; Zhang, M.; Wang, Q.; Du, A.; Wang, H.; Liu, G.; Wang, L. Organic−Inorganic Bismuth (III)-Based Material: A Lead-Free, Air-Stable and Solution-Processable Light-Absorber beyond Organolead Perovskites. *Nano Res.* **2016**, *9*, 692−702.
(40) Ganose, A. M.; Savory, C. N.; Scanlon, D. O. Electronic and Defect Properties of $(CH_3\ NH_3)_2\ Pb(SCN)_2\ I_2$ Analogues for Photovoltaic Applications. *J. Mater. Chem. A* **2017**, *5*, 7845−7853.
(41) Maughan, A. E.; Ganose, A. M.; Candia, A. M.; Granger, J. T.; Scanlon, D. O.; Neilson, J. R. Anharmonicity and Octahedral Tilting in Hybrid Vacancy-Ordered Double Perovskites. *Chem. Mater.* **2018**, *30*, 472−483.
(42) Du, M. H. Efficient Carrier Transport in Halide Perovskites: Theoretical Perspectives. *J. Mater. Chem. A* **2014**, *2*, 9091−9098.
(43) Xiao, Z.; Meng, W.; Wang, J.; Mitzi, D. B.; Yan, Y. Searching for Promising New Perovskite-Based Photovoltaic Absorbers: The Importance of Electronic Dimensionality. *Mater. Horiz.* **2017**, *4*, 206−216.
(44) Yu, L.; Zunger, A. Identification of Potential Photovoltaic Absorbers Based on First-Principles Spectroscopic Screening of Materials. *Phys. Rev. Lett.* **2012**, *108*, 068701.
(45) Savory, C. N.; Walsh, A.; Scanlon, D. O. Can Pb-Free Halide Double Perovskites Support High-Efficiency Solar Cells? *ACS Energy Lett.* **2016**, *1*, 949−955.
(46) Ganose, A. M.; Savory, C. N.; Scanlon, D. O. Beyond Methylammonium Lead Iodide: Prospects for the Emergent Field of Ns^2 Containing Solar Absorbers. *Chem. Commun.* **2017**, *53*, 20−44.
(47) Stupak, A. P.; Blaudeck, T.; Zenkevich, E. I.; Krause, S.; Von Borczyskowski, C. The Nature of Non-FRET Photoluminescence Quenching in Nanoassemblies from Semiconductor Quantum Dots and Dye Molecules. *Phys. Chem. Chem. Phys.* **2018**, *20*, 18579−18600.
(48) Abdi-Jalebi, M.; Andaji-Garmaroudi, Z.; Cacovich, S.; Stavrakas, C.; Philippe, B.; Richter, J. M.; Alsari, M.; Booker, E. P.; Hutter, E. M.; Pearson, A. J.; Lilliu, S.; Savenije, T. J.; Rensmo, H.; Divitini, G.; Ducati, C.; Friend, R. H.; Stranks, S. D. Maximizing and Stabilizing Luminescence from Halide Perovskites with Potassium Passivation. *Nature* **2018**, *555*, 497−501.

DOI: 10.1021/acsaem.8b01809
ACS Appl. Energy Mater. XXXX, XXX, XXX−XXX